CMOS Microflow Cytometer for Magnetic Label Detection and Classification

Pramod Murali, *Member, IEEE*, Ali M. Niknejad, *Fellow, IEEE*, and Bernhard E. Boser, *Fellow, IEEE*

Abstract—A flow cytometer chip fabricated in 65-nm standard CMOS technology embedded into a microfluidic channel is presented. The chip detects cells specifically tagged with magnetic labels by demodulating the change in coupling between an excitation coil and a pickup coil of a differential spiral transformer. Operation of the flow cytometer cartridge is verified for the detection of SKBR-3 breast cancer cells tagged with manganese ferrite magnetic labels using EpCAM-biotin-streptavidin chemistry. Magnetic labels of different materials are classified by the difference in the phase of their complex susceptibility.

Index Terms—Biosensor, CMOS, flow cytometer, magnetic, microfluidics, miniature.

I. Introduction

FLOW cytometers are instruments that can detect and classify specific cells in a biological sample. They are extensively used in medical diagnostics, such as hematology, HIV detection, and so on [1]. They are also used for pathogen monitoring in food industry and water supply. Many researchers have considered label-free chip scale flow cytometers [2]–[9]; however, our focus here is label-based formats since it has been shown to offer superior performance than label-free techniques [10]. The current approach to flow cytometry in diagnostics involves: 1) collection of a blood sample from the patient; 2) treatment of the sample with an anticoagulant and lysing agent followed by dilution; 3) labeling of the cells of interest with antibody conjugated fluorescent molecules or staining agents; and 4) running the sample through an optical flow cytometer. The instrument contains one or more lasers that excite the fluorophores on the cells as they pass through the laser beam one at a time in a carrier fluid. The scattered and fluorescent light is amplified by photomultipliers and detected by photodetectors. The acquired data are subsequently processed to detect and classify the cells based on surface markers (fluorescent light) and granularity (scattered light).

A key limitation of this approach is the use of fluorescent molecules which necessitates elaborate sample preparation such as lysing of red blood cells (RBCs). This step is necessary because the RBCs will autofluorescence and interfere with optical measurement. An unlabeled sample of cells is also used to calibrate the instrument and set the threshold for the photodetectors in the instrument to minimize false detection.

Recently, there have been efforts to replace the fluorescent labels with magnetic labels to enable miniature flow cytometers [11]–[17]. Fundamentally, the biological sample is not magnetic ($\chi = 10^{-5}$) and does not interfere with the detection of magnetic labels ($\chi = 0.1 - 2$). Therefore, flow cytometry can be performed in whole blood without the need for RBC lysis or calibration steps [12]. Giant magnetoresistance (GMR) [11], [12], superconducting quantum interference devices [13], and μHall sensors [14] in non-CMOS technologies have been reported for biosensing with magnetic labels. With CMOS sensors, the sensitivity of LC tank based sensors [15], [16] is inadequate for flow cytometry while Hall sensors [17] require CMOS postprocessing steps. Furthermore, it is also important to discriminate between different magnetic labels similar to the colors of fluorescent labels. In addition to reducing analysis time, sample and reagent volume, multiple labels can be used to specifically recognize cell subtypes or rare-cells, detect multiple cell types in the same sample, and distinguish live cells from the dead ones [14].

In this paper, we demonstrate a magnetic flow cytometer fabricated in the standard CMOS technology with integrated microfluidics as a *first step* toward a miniature flow cytometer. It is also important to consider factors, such as label storage at room temperature, biological sample-to-sample variations, variations arising from sample collection procedure, long-term stability of microfluidic channel surfaces, effect of device contamination on the assay, and so on, to realize a complete *clinically relevant* magnetic flow cytometer; however, these topics are beyond the scope of this paper. The rest of this paper is organized as follows. Magnetic labels are described in Section II followed by a discussion of design requirements for a typical miniature flow cytometer in Section III. Section IV details the design of the sensor and Section V discusses the architecture of the CMOS chip for processing the sensor signals. Integration of the chip with a microfluidic channel is presented in Section VI. Measurement results are presented in Section VII and Section VIII concludes this paper.

II. Magnetic Labels

The magnetic labels used in this paper consist of single domain (5–20 nm) ferromagnetic nanoparticles embedded in a polymer matrix of 1 or 4.5 μm diameter. The thermal energy at room temperature is sufficient to randomize the net direction of magnetic moment of these single domain nanoparticles. The magnetic moment within the particles aligns to the applied external magnetic field giving rise to four or five orders of magnitude higher susceptibility than paramagnetic materials ($\chi \approx 10^{-5}$). This mechanism of magnetism is often referred to as superparamagnetism. The susceptibility ($\chi = \chi' - j\chi''$) of
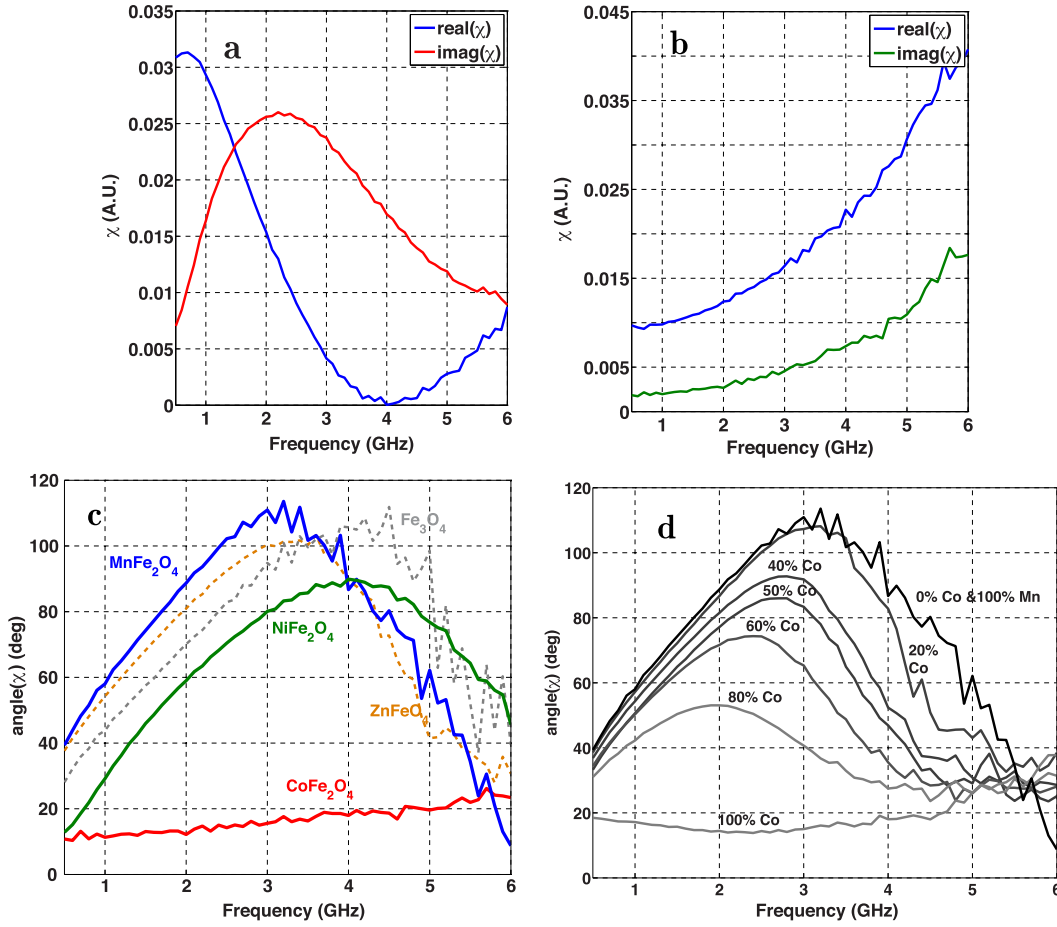
Fig. 1. (a) Complex susceptibility plot for iron oxide nanoparticles. (b) Complex susceptibility plot for cobalt ferrite nanoparticles. (c) Phase of complex susceptibility of different magnetic materials. (d) Phase of complex susceptibility for different titrations of nanoparticles.

these magnetic labels is a frequency- and material-dependent complex number [18].

Plots of the complex susceptibility of iron oxide and cobalt ferrite nanoparticles are shown in Fig. 1(a) and (b), respectively. Fig. 1(c) shows a plot of the phase of the susceptibility for different kinds of nanoparticles. The phase difference can be used for classifying magnetic labels similar to colors in fluorescent molecules. The peaking in the imaginary component of susceptibility (χ'') is due to *ferromagnetic resonance* and the corresponding frequency is a weak function of the size of the nanoparticles [19]. This is unlike *Neel's relaxation* phenomenon observed at lower frequencies (≈ 5–100 kHz), where $\chi(\omega)$ is an exponential function of the size of the nanoparticles [18]. Therefore, label classification at lower frequency using Neel's relaxation phenomenon is almost impractical considering the wide distribution of nanoparticle sizes arising from the fabrication process variations. As a consequence, it is important to operate the sensor in the ferromagnetic resonance regime, 1–5 GHz. Shown in Fig. 1(d) are the measurement results of different titrations of manganese ferrite and cobalt ferrite nanoparticles. The plot of the mixtures shows that the phase interpolates well between the phase plots of 100% of each type of nanoparticles. These plots are important to consider if two label classes are bound to the same cell.

III. CYTOMETER DESIGN REQUIREMENTS

The design of miniature flow cytometers involves the design of a sensor for detecting the labeled cells, the design of microfluidics to carry the cells over the sensor, and, finally, the design of a sequence of process steps to integrate the sensor with the microfluidics. Each application scenario demands a different set of SNR (false alarms) and throughput (cells/s) requirements from the cytometer.

Let us consider SKBR-3 breast cancer cell counting as one such application to illustrate the steps necessary to determine the SNR and throughput requirements for a flow cytometer. Let us assume that we have already concentrated these cells to about 200 cells/μL and that it is sufficient to determine the count value with a CV[1] $\leq 5\%$.

We start by defining a measurement duration $T_{\text{meas}} \leq 2$ min as convenient value. A sample volume of about 5 μL contains $N_S = 1000$ SKBR-3 cells that needs to be counted with an accuracy CV $\leq 5\%$. The microchannel dimensions can be suitably designed to carry the 5-μL sample in 2 min at a flow rate of ≈ 40 nL/s. For reference, a commercial optical cytometer scans through hundreds of thousands of cells using high-speed optics, sensitive photomultipliers, syringe pumps,

---

[1]CV: coefficient of variation is defined as the ratio of standard deviation to the mean value
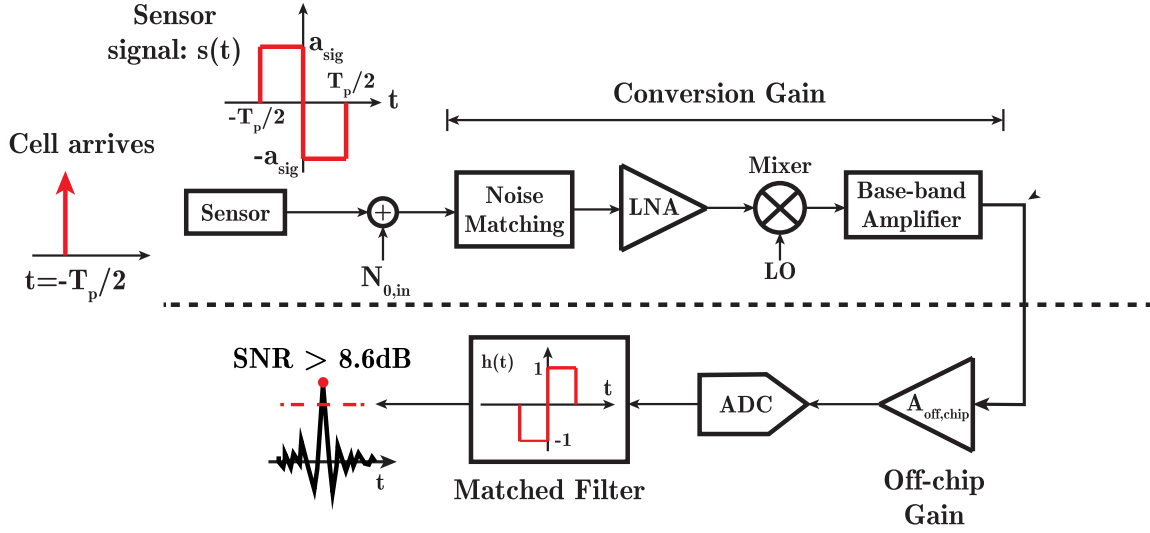
Fig. 2. Schematic of flow cytometer receiver chain.

and so on, because this instrument has to look at every single cell passing through the laser. A bench-top instrument (such as BD Accuri) has a flow rate of 160 nL/s–1.6 μL/s [20]. However, a magnetic cytometer detects only the labeled cells, the unwanted-unlabeled cells can flow undetected anywhere in the microchannel. Therefore, it is important to recognize here that this device is useful for specific applications and cannot be a complete replacement to an optical cytometer. The flow rate can be improved, if necessary, by having multiple parallel microfluidic channels with each having a separate CMOS sensor.

To obtain the SNR requirements for the cytometer from the CV constraints, it is necessary to look at the complete signal path, which includes the sensor, receiver circuitry, a matched filter, and a threshold detector, as shown in Fig. 2. The flow of a cell over the sensor produces a bipolar pulse at its output, which is then amplified by the receiver. To maximize the SNR, the receiver output is convolved (or autocorrelated) with the expected pulse shape using a matched filter (whose impulse response is identical to the shape of the pulse from the sensor). We eventually conclude that a magnetically labeled cell is detected by the cytometer if the matched filter output exceeds a certain threshold. However, the presence of noise in the system ($N_{0,in}$) leads to false positives or background counts. Counting statistics from radiation detection theory [21] can be used to determine the appropriate threshold or the minimum SNR[2] required to meet the accuracy requirements as explained in the following.

Assume that a background count (N_B), the count obtained by the cytometer due to random noise in the system when there are no labeled cells flowing over the sensor, is repeatedly measured for a fixed duration T_{meas} for a certain threshold setting.[3] The count will be Poisson distributed with mean N_B and $\sigma_{N_B} = (N_B)^{1/2}$. Now, if we repeat the experiment in the presence of labeled cells flowing over the sensor, we will
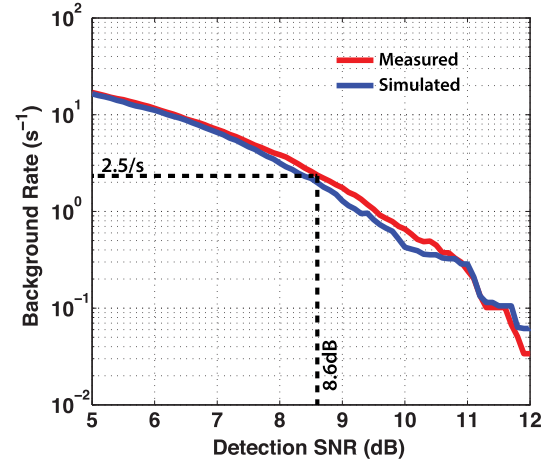

Fig. 3. Background rate versus SNR (threshold).

count both the background as well as the cells to obtain a total count (N_T) and $\sigma_{N_T} = \sqrt{N_T}$. N_T and N_B can then be used to determine the actual number of cells (N_S). $N_S = N_T - N_B$, $\sigma_{N_S} = (N_S + 2N_B)^{1/2}$

$$\text{CV} = \frac{\sigma_{N_S}}{N_S} = \frac{\sqrt{N_S + 2N_B}}{N_S}. \tag{1}$$

Using (1), we can determine the maximum permissible background count as $N_B = 300$ or a count rate of 2.5/s (count rate = N_B / T_{meas} with $T_{meas} = 2$ min) for $N_s = 1000$ SKBR-3 cells in the sample and CV = 4%. Using the background count rate versus threshold plot for our system shown in Fig. 3, we need SNR greater than 8.6 dB (threshold) from the labeled SKBR-3 cells to meet the accuracy requirements. The background count rate plot in Fig. 3 is obtained by counting the number of times the match filter output exceeds a given threshold and normalizing this count value by the duration of the measured data.

IV. SENSOR

A. Sensor Modeling

In this section, we present the design of a magnetic label sensor that incorporates a magnetizing coil (L_1) and a pickup

---

[2]SNR is defined as the ratio of peak value of the signal to rms noise after matched filtering.

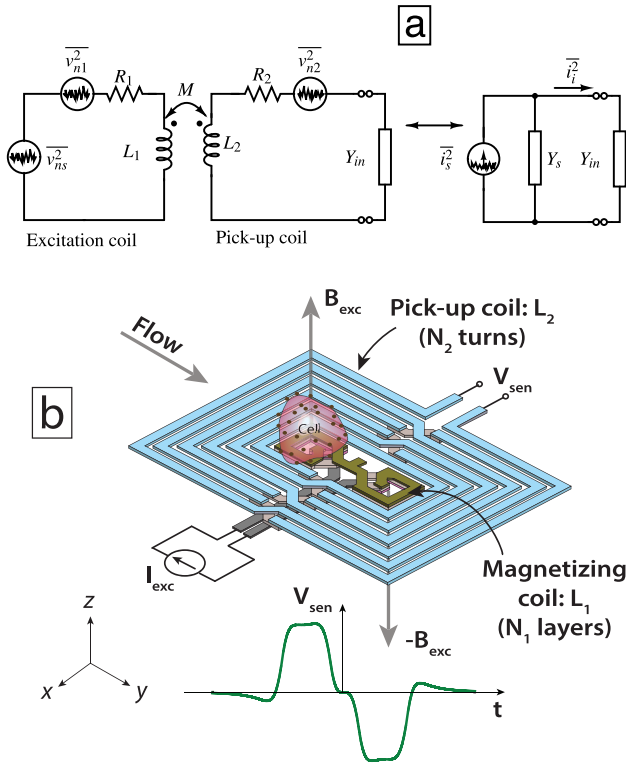[3]Here, *threshold* is defined (in decibels) relative to rms noise at the match filter output

Fig. 4. (a) Model of spiral sensor and its different noise sources. (b) Schematic of the sensor.

coil (L_2) to sense the magnetic moment induced in the labels [see Fig. 4(a)]. Our goal is to maximize the SNR from the sensor by appropriate design of inductances L_1 and L_2. The mutual inductance M arises from the magnetic coupling and it is modulated by the labels. The magnetic field that magnetizes the labels when the cell is over the center of excitation spiral (L_1) can be approximated as [see Fig. 4(b)]

$$\overrightarrow{H_{\text{exc}}} = \frac{\overrightarrow{B_{\text{exc}}}}{\mu_0} = N_1 \frac{2\sqrt{2} \cdot I_{\text{exc}}}{\pi d_1} \hat{k} \qquad (2)$$

where $\overrightarrow{H_{\text{exc}}}$ is the excitation magnetic field intensity, $\overrightarrow{B_{\text{exc}}}$ is the excitation magnetic field density, μ_0 is the permeability of free space, I_{exc} is the current in L_1, N_1 is the number of metal layers, d_1 is the diameter of the loop, and $\hat{k}$ is the unit vector along the z-axis normal to plane of the coil. Magnetic labels bound on the cell, each of volume V, and susceptibility (χ), when magnetized by $\overrightarrow{H_{\text{exc}}}$, will have a magnetic moment ($\vec{m} = \chi V \overrightarrow{H_{\text{exc}}}$) and generate a magnetic field density ($\overrightarrow{B(r)}$) in the space around the cell

$$\overrightarrow{B(r)} = \frac{\mu_0}{4\pi |\overrightarrow{r}|^3}(3(\vec{m} \cdot \hat{r})\hat{r} - \vec{m}) \qquad (3)$$

where $\overrightarrow{r} = \hat{r}.|\overrightarrow{r}|$ is the distance vector from the center of the label to a point in space. $\overrightarrow{B(r)}$ couples to the pickup coil (L_2) and the mutual inductance (M) is given by

$$M = \frac{\phi_2}{I_{\text{exc}}} \qquad (4)$$

where

$$\phi_2 = \sum_{j=1}^{N_2} \sum_{i=1}^{P} \int_{A_j} \overrightarrow{B_i(r)} \cdot \overrightarrow{dS}$$

A_j is the area of each loop of the N_2 loops in the pickup coil and P is the number of magnetic labels on a cell, $\overrightarrow{dS}$ is the infinitesimal area element in the $\hat{k}$-direction. Here, we assume that magnetic labels bound on the cell do not interact with each other, and hence, the total magnetic field density is the sum of individual contributions from the labels [11].

B. Sensor Design Considerations

Fig. 4(a) also shows the different noise sources in the sensor. The series resistors of L_1 and L_2 are modeled by R_1 and R_2, respectively. $\overline{v_{ns}^2}$ is the thermal noise generated by the buffers driving the excitation coil L_1 and $\overline{v_{n1}^2}$ and $\overline{v_{n2}^2}$ are thermal noise sources from the resistances R_1 and R_2, respectively. It will be convenient to combine all the noise sources into $\overline{i_s^2}$ and equivalent source admittance Y_S as shown in Fig. 4(a) (right). The sensor is connected to a receiver with input admittance Y_{in}. If we assume that the $Q = \omega L/R$ of the excitation coil is large ($Q_1^2 \geq 10$), it can be shown that the noise ($\overline{i_{i,\text{noise}}^2}$) to signal ($\overline{i_{i,\text{sig}}^2}$) ratio at the input of the receiver is

$$\frac{N}{S} = \frac{\overline{i_{i,\text{noise}}^2}}{\overline{i_{i,\text{sig}}^2}} = \frac{L_1}{k_c^2 L_2} \frac{\overline{v_{n2}^2}}{\overline{v_{\text{sig}}^2}} + \frac{\overline{v_{ns}^2} + \overline{v_{n1}^2}}{\overline{v_{\text{sig}}^2}} \qquad (5)$$

where $k_c = M/(L_1 L_2)^{1/2}$ is the coupling coefficient, $\overline{v_{\text{sig}}^2}$ is the power of voltage source that drives the excitation coil. From (5), we can see that the noise from the excitation source $\overline{v_{ns}^2}$ and excitation coil resistance $\overline{v_{n1}^2}$ has a direct impact on the SNR. $\overline{v_{n1}^2}$ can be reduced by implementing L_1 on top metal layers of the CMOS process and $\overline{v_{ns}^2}$ can be reduced by reducing the phase noise of the oscillator driving the sensor. In addition, the SNR can be further improved by a smaller excitation coil inductance (L_1), a large pickup coil inductance (L_2), and increasing coupling coefficient (k_c) as detailed in the following.

1) Excitation Coil Design L_1: From (2), we see that the magnetic field strength increases inversely with decreasing diameter of the excitation coil. However, if the size of the excitation coil is significantly smaller than that of the cell (which is typically 15 μm), the coil can be approximated by an infinitesimal magnetic dipole whose magnetic field strength drops as $1/r^3$. Hence, the labels attached on the surface of the cell that are far from the center of this infinitesimal excitation coil will experience a weak or insufficient magnetizing field. Therefore, for a given current through the excitation coil, the optimum diameter that will maximize the magnetic moment induced in the labels is close to the size of a cell, i.e., 15 μm [22].

2) Pickup Coil Design L_2: The width, spacing, and the number of turns of the pickup coil (L_2) impact the SNR of the sensor. With the increasing number of turns, the magnetic flux picked up by L_2 increases with diminishing returns. In the limiting case of a very large pickup coil and a cell placed at its center, all the magnetic flux lines of the cell will loop back to itself inside the coil causing no effective flux to pass through the pickup coil. In other words, no voltage will be induced in the pickup coil. Moreover, the series resistance R_2 increases linearly with the number of turns decreasing
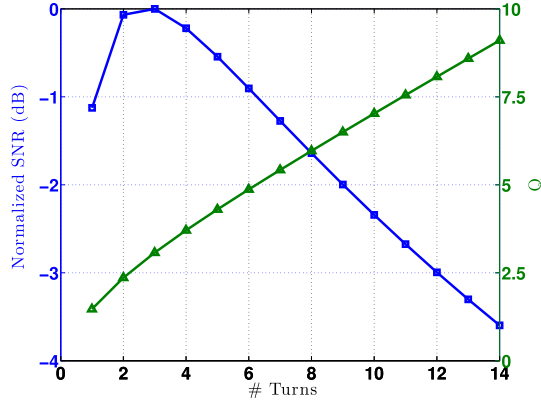
Fig. 5. Effect of number of turns in the pickup coil (L_2) on the SNR and Q.
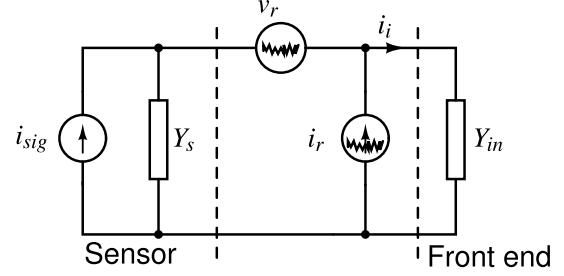

Fig. 6. Sensor connected to the front end with input referred instantaneous correlated noise current i_r and noise voltage v_r.

the SNR. From simulations shown in Fig. 5, we see that three turns in L_2 maximize the SNR of the sensor. However, choosing more than three turns increases the inductance and quality factor Q. A higher Q is advantageous for boosting the voltage signal at the input of the front-end amplifier by series resonance with amplifier input capacitance. We have chosen six turns in our design which causes only 0.8-dB penalty over the maximum SNR. Reducing the spacing between turns also increases the SNR but the minimum spacing is limited by the process technology.

3) Coupling Coefficient k_c: It is desirable to increase the coupling coefficient as seen in (5). k_c depends on: 1) the vertical separation of the cell from sensor surface; 2) product of the susceptibility and frequency of operation $\omega\chi(\omega)$; and 3) the amount of magnetic labels bound to the cell. First, the separation of the cell from the sensor can be reduced by magnetophoresis [23], [24]. Second, the choice of frequency of operation for the sensor depends on the type of magnetic labels due to the frequency dependence of $\chi(\omega)$. For instance, iron oxide is the most commonly available magnetic label class since it is a nontoxic material. Choosing an operating frequency of 2.6 GHz maximizes $\omega\chi(\omega)$ for these labels. Finally, the coupling coefficient also depends on the amount of magnetic labels bound on the cell. During design phase, it is difficult to estimate the number of labels bound on a cell, because it depends on the diffusion rate of labels toward the cells, steric-hindrance effects that prevent the labeling process, Brownian-motion of the labels, surface antigen expression on the cells, cell culture conditions, pH of the labeling buffer solution, temperature, and so on. Therefore, the optimum conditions have to be experimentally determined to maximize the binding of labels onto cells. As a consequence, assumptions have to be made on the number of labels bound on a cell during sensor design phase to estimate the coupling coefficient and consequently the value of the SNR from the sensor.

4) Effect of Saline Loss on Sensor Performance: The cells have to be dispersed and carried over the sensor in a saline solution [phosphate buffered saline (PBS)]. The presence of dissolved salts in saline causes high frequency loss and de-Qing of the spiral inductors. This manifests as an increase in R_1 and R_2 and, hence, $\overline{v_{n1}^2}$ and $\overline{v_{n2}^2}$ [see Fig. 4(a)]. We have modeled the lossy dielectric properties of saline

using semiempirical expressions in [25] and incorporated these models into full-wave EM simulations.

C. Sensor Implementation

Using the insights gained from the analytical models, a spiral sensor is implemented as shown in Fig. 4(b). The magnetizing coil is a three layer, single turn per layer spiral inductor implemented in the top three metal layers of the CMOS process and has an inductance of 490 pH. A center tap is provided for dc biasing the excitation coil driver circuit (discussed in Section V-C). 100 mA$_{pp}$ of excitation current is used to magnetize the labels with magnetic field density of 9.4 mT (simulated) to meet the SNR requirements. The inner diameter is 15 μm which is comparable to the size of a typical SKBR-3 cell and the metal trace width is 6 μm to limit the temperature raise from Joule heating to less than 15 °C in air. A 15 °C increase of temperature in air (assuming 22 °C ambient temperature) limits the final temperature of the fluid to less than 37 °C. The maximum final temperature is limited to about 42 °C after which the cells get damaged [26], which is undesirable if they have to be harvested downstream for further analysis. Apart from undesirable heat generation, larger excitation currents can also lead to stiction of labels on the sensor by magnetophoresis.

The pickup coil (L_2) is a symmetric six turn spiral implemented on top two metal layers connected in parallel and has an inductance of 4.87 nH. Minimum width and spacing between turns, limited by process technology, maximize the flux picked up from the labels. Adding more turns for larger flux pickup is compromised by thermal noise from series resistance and overall size of the coil. The sensitivity of the sensor is 0.14 V/mT/GHz (simulated). The simulated output of the sensor as the cell flows over it is also shown in Fig. 4(b). For the purpose of analysis, the pulse shape of sensor output can be approximated by a bipolar rectangular pulse as shown in Fig. 2.

V. RECEIVER DESIGN

The signal from the pickup coil needs to be down-converted to baseband for further amplification, digitization, and processing. Among different receiver architectures, a direct down conversion receiver offers low power and high level of integration [27], [28].

A. Front-End Noise Matching

Let us consider the noise model of the receiver front end as shown in Fig. 6. Our goal is to minimize its noise contribution.
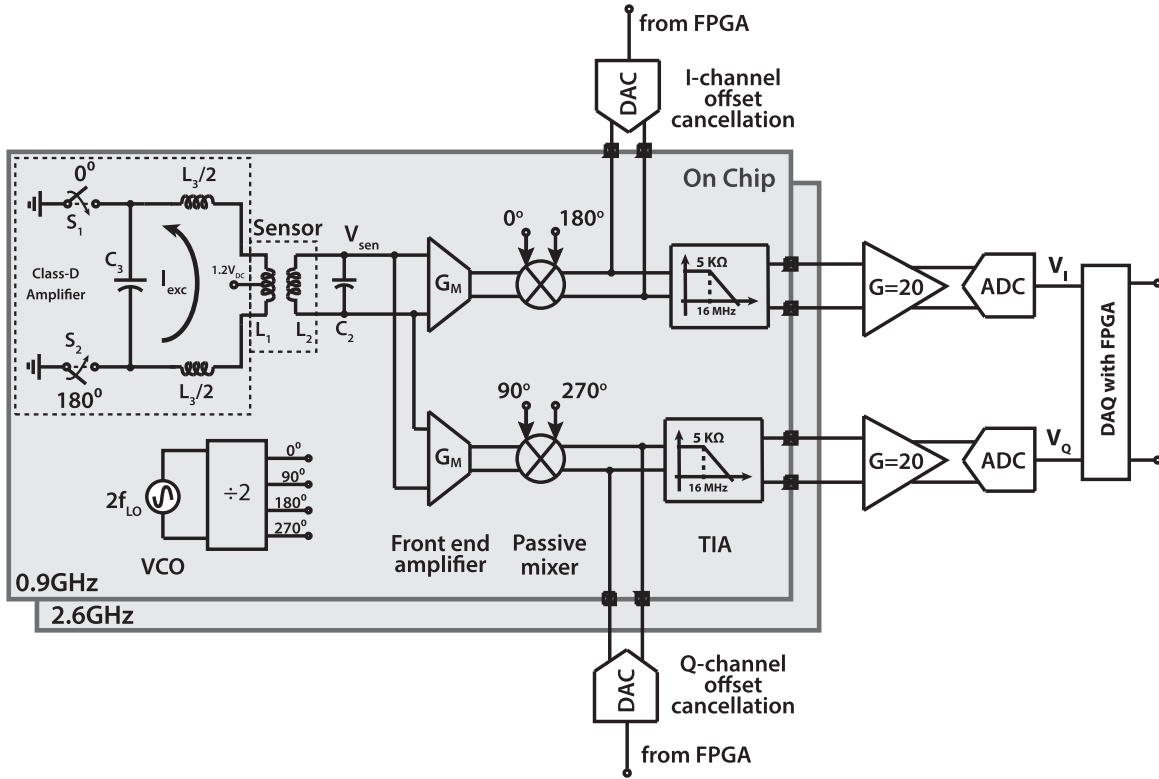
Fig. 7.   Architecture of the chip.

Here, i_r and v_r are instantaneous input referred correlated current noise and voltage noise sources of the receiver such that $i_r = Y_c v_r$, where Y_c is the correlation coefficient.

The noise to signal ratio at the input of the front end will be

$$\frac{N}{S} = \frac{\overline{i_{i,\text{noise}}^2}}{\overline{i_{i,\text{sig}}^2}} = \frac{\overline{v_r^2}}{\overline{i_{\text{sig}}^2}} |Y_c + Y_s|^2. \tag{6}$$

From (6), we can improve the SNR by either reducing $\overline{v_r^2}$ which translates to increasing the power consumption in the front end amplifier or by reducing $|Y_c + Y_s|^2$ as discussed in the following.

To find Y_c, let us consider an MOSFET front-end and let its noise be modeled by a current noise generator $(\overline{i_d^2})$ connected between its drain and source terminals. Using the instantaneous noise current of the MOSFET (i_d), we get

$$i_r = \frac{j\omega C_{gs}}{g_m} i_d$$
$$v_r = \frac{i_d}{g_m}$$
$$Y_c = \frac{i_r}{v_r} = j\omega C_{gs}. \tag{7}$$

From (7), we see that Y_c is a small capacitive admittance (positive) determined by C_{gs} of the MOSFET. Noting that Y_s is the inductive admittance (negative) of the pickup coil, we can increase Y_C by adding a capacitor (C_{add}) in parallel to C_{gs} such that the reactive components of Y_s and Y_c cancel each other and minimize $|Y_s + Y_c|^2$. When this happens, the pickup coil (L_2) will resonate with the total capacitance ($C_{gs} + C_{\text{add}}$) at the frequency of operation.

In other words, this additional capacitance will effectively boost the voltage (by a factor Q) induced in the pickup coil at the gate of the front-end transistors. An alternate approach is to increase the size of the input transistors such that C_{gs} alone will resonate with L_2 (without any additional C_{add}). A larger input device provides higher g_m and lower input referred thermal noise for the same bias current. However, this is not done as part of this paper.

B. Multifrequency Label Detection

Operating two or more sensors at the same frequency but separated spatially provides an SNR improvement [29]. With N sensor array elements, the signal amplitude and noise power scale with N, as a consequence, SNR improves by $N/\sqrt{N} = \sqrt{N}$. As labeled cells flow through the microchannel, vertical magnetophoresis (using a magnet beneath the chip) tries to ensure that the cells get pulled close to the surface of the sensor. However, due to surface roughness and fluid velocity gradients, the cells can get pushed away from the sensor and miss detection events. Having multiple sensing sites increases the chances of detection of cells by a given sensor as shown later in measurement results. In addition, if we operate the sensor elements of the array at multiple frequencies, there are two other benefits.

First, the strength of the signal from the sensor scales linearly with the frequency of operation. This is particularly beneficial for cobalt like nanoparticles where the magnitude of susceptibility is increasing between 1 and 5 GHz [see Fig. 1(b)]. Second, multifrequency interrogation can also be used to improve the classification accuracy of different magnetic label classes.
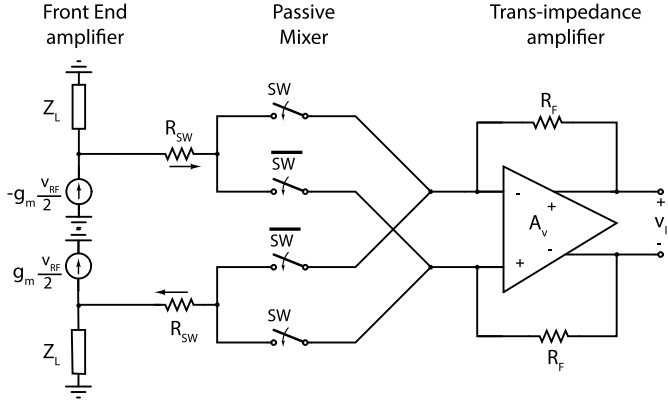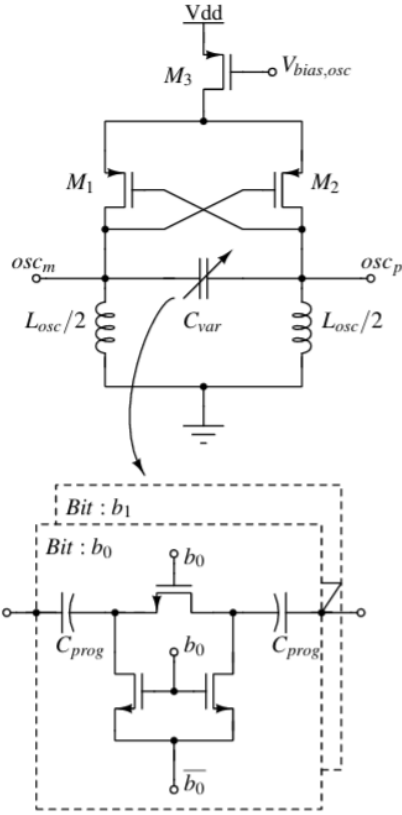
Fig. 8. Schematic of receiver chain.

Fig. 9. Circuit schematic of oscillator.

Fig. 10. Drive circuit for excitation coil.

Finally, the heat dissipation of an array of N elements is a factor N higher than that of a single element. However, this is offset by proportionally smaller thermal resistance due to increase in chip area. Second, the flow of liquid over the chip assists in additional heat dissipation. This being said, the maximum possible power dissipation is also limited by packaging materials, number of wire-bonds that can carry the heat away, and fluid flow rate all of which depend on the specific application.

C. Circuit Implementation

The complete architecture of the chip is shown in Fig. 7. The G_M block is the front-end amplifier that converts the sensor voltage signal to current before down conversion to baseband by a passive mixer. The baseband current is converted to a voltage by a transimpedance amplifier (TIA). The conversion gain
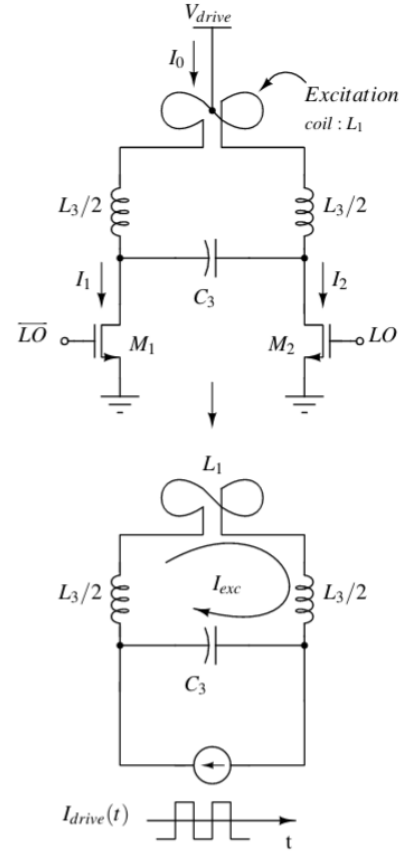
of the whole receiver chain schematically shown in Fig. 8 is

$$\text{Conv. Gain} = \frac{v_{\text{IF}}}{v_{\text{RF}}} = \left(\frac{2}{\pi}\right)\left(\frac{R_F Z_L g_m}{Z_L + R_{SW} + R_F/A_v}\right) \quad (8)$$

R_F is the feedback resistor of the TIA, Z_L and g_m are the output impedance and transconductance of the front-end amplifier, R_{SW} is the on-resistance of the passive mixer switches, and A_v is the voltage gain of the opamp in the TIA. To improve the conversion gain in (8) for a given g_m and R_F, it is important to minimize R_{SW} and increase A_v and Z_L in the design of the receiver. The following sections Sec. V-C1 through Sec. V-C7 describe describe the design of each of the individual blocks shown in Fig. 7.

1) Oscillator: The oscillator running at twice the LO frequency is implemented using an *LC* tank connected to a pMOS ($M_{1,2}$) based negative transconductance stage as shown in Fig. 9. Two bits ($b_{1,0}$) of digital frequency programming are provided to modify the oscillation frequency by $\approx 20\%$ using a capacitor bank.

The sinusoidal output of the oscillator is converted to a square wave by ac coupling it to an inverter. The outputs of the inverters drive the clock inputs of toggle flip-flops to generate in-phase and quadrature phases of LO signals. Buffers are added at the output of the flip-flops to drive the mixer and excitation coil driver switches. The digital blocks, such as buffers, flip-flops, and so on, are implemented using the standard cell digital library. An open drain transistor is connected to the divider outputs for off-chip frequency measurement.
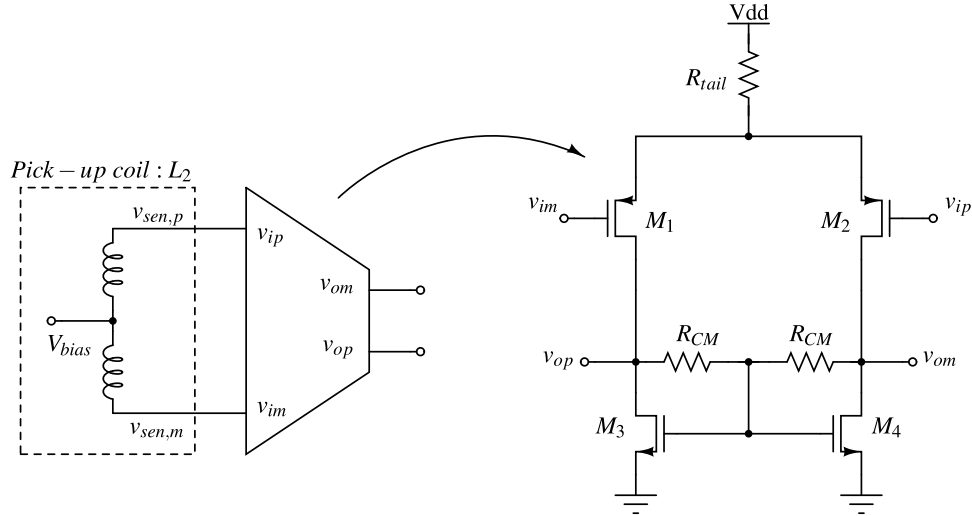
Fig. 11.   Front-end amplifier circuit.

2) Excitation Coil Driver: Circuit for driving the excitation coil is shown in Fig. 10. The switches $S_{1,2}$ shown in Fig. 7 are realized using nMOS transistors ($M_{1,2}$). The excitation coil (L_1) is driven by a class-D amplifier formed by $M_{1,2}$, L_3, and C_3. The center tap of the differential excitation coil is connected to the drive voltage (V_{drive}) and the maximum current through the transistors $M_{1,2}$ is determined by their on-resistance and V_{drive}. The LC tank formed by $L_3 + L_1$ resonates at the LO frequency with the capacitor C_3 boosting (by a factor Q) the current $I_{\text{drive}} = (I_1 - I_2)/2$ through the excitation coil by parallel resonance. L_3 is implemented as a symmetric spiral inductor on M8 and M9 metal layers of the ten metal CMOS process and is isolated from oscillator using a guard ring. Dummy metal fill ($2.1 \times 2.1 \ \mu\text{m}^2$) in all the metal layers is added inside the spiral to meet the fabrication constraints. The gates of M_1 and M_2 are driven by the in-phase outputs of the clock divider.

3) Front-End Amplifier: The front-end amplifier converts the voltage induced in the pickup coil into a current using a single-stage transconductor circuit shown in Fig. 11. The input referred thermal noise floor of the receiver chain is minimized by designing the pMOS input transistors ($M_{1,2}$) for 20 mS transconductance using 2.2 mA bias current through each of them. The bias voltage to the gate of the input transistors is provided through the center tap of the pickup coil. The gate bias to nMOS current source load transistors ($M_{3,4}$) is provided by a resistive divider common mode detection circuit ($R_{\text{CM}} = 3.6 \ \text{k}\Omega$).

4) Passive Mixer: We have chosen a passive mixer because it has better linearity and lower flicker noise compared with an active Gilbert-cell mixer. The switches of the passive mixer are implemented with nMOS transistors. The output current of the front-end amplifier is ac coupled to the RF input port of the mixer using 8 pF capacitors. The square wave ($0 - V_{\text{dd}}$) from the divider is ac coupled to the gates of the mixer switches. The gates are biased at V_{dd} so that the switches have a nominal on-resistance of 10 Ω, three times lower than the input impedance of the TIA.

5) Baseband Amplifier: The baseband stage is a TIA that is realized using an opamp with a resistor ($R_F = 5 \ \text{k}\Omega$) and a capacitor ($C_F = 2$ pF) in feedback as shown in Fig. 12. The opamp is a fully differential two-stage amplifier circuit with the input stage realized using nMOS transistors ($M_{1,2}$). Each input transistor is biased with 0.2 mA to give $g_m = 2.2$ mS. The pMOS second gain stage ($M_{6,7}$) is designed to drive a load capacitor of 10 pF which accounts for off-chip PCB trace capacitance and off-chip gain stage input capacitance. The length of the input transistors is designed to have a flicker noise corner frequency of 8 kHz. The common mode outputs of the first stage and second stage are set using two separate common-mode feedback (CMFB) loops. The first-stage CMFB uses two differential pairs and the second-stage CMFB uses a resistive divider to detect the common-mode voltages, respectively [30]. The stability of the opamp is ensured using a Miller capacitor (C_c) in series with a resistor (R_z) that cancels the right half-plane zero. The overall TIA has input impedance of 34 Ω and 3 dB bandwidth of 660 kHz.

6) Feed-Through Cancellation: The pickup coil encloses the excitation coil with a gap of 3 μm. This cause undesirable capacitive coupling between the two coils. This steady-state coupling signal will be down-converted to a dc current by the mixer. The dc offset current has to be canceled out in order to prevent the saturation of the baseband amplifier or subsequent off-chip amplifier stages. An external DAC is used to feed a programmable dc current to the input of the TIA to cancel this offset current as shown in Figs. 7 and 12.

7) Chip Fabrication: The need to integrate the chip with the microfluidic channel imposes additional constraints on the layout design of the chip. The pads are placed only on the two opposite sides of the chip so that the wire-bonds do not interfere with the fluid flow. Second, the sensor is placed close to the center of the chip to avoid leakage near the interface between the chip edge and the microfluidic channel. For the multiple frequency of operation, the power supplies are isolated to avoid any injection locking between different channels. The circuits are implemented in 65-nm CMOS technology. Two frequency channels (0.9 and 2.6 GHz) are designed with each channel occupying an active area of $1.5 \times 0.45 \ \text{mm}^2$ as shown in Fig. 13.
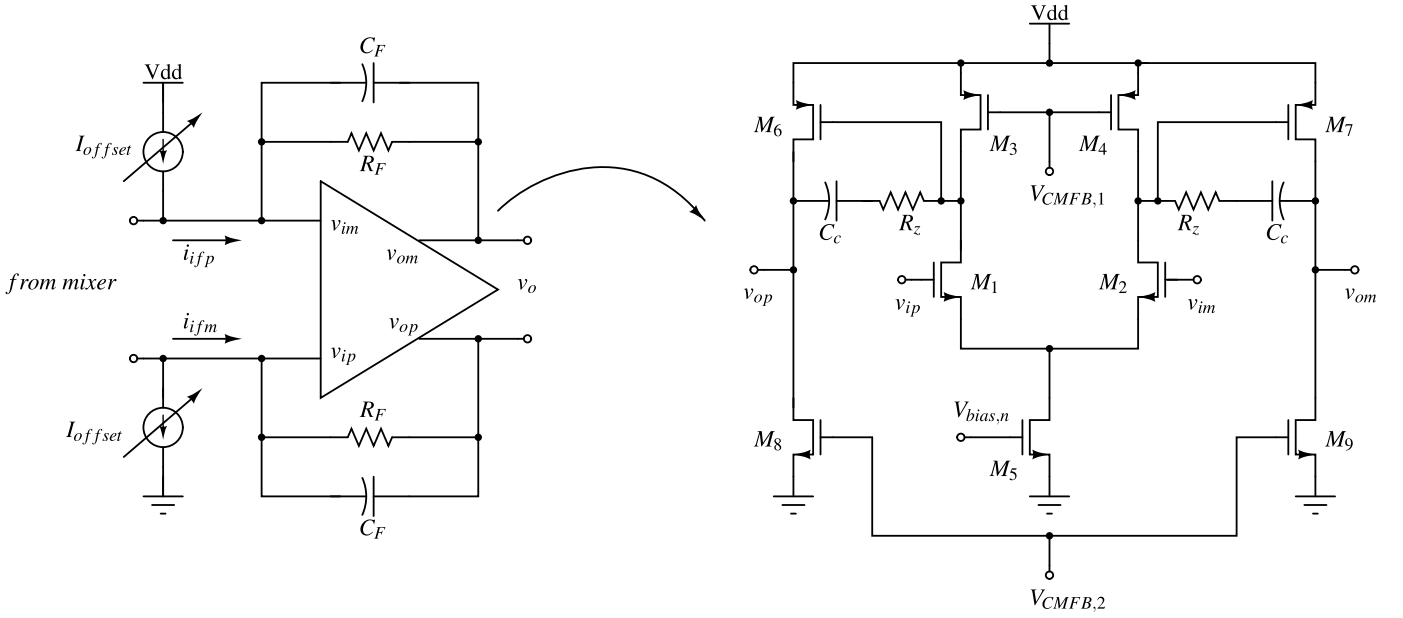
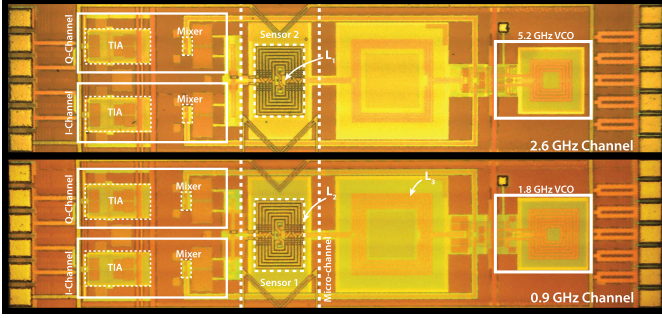Fig. 12.   Circuit schematic of TIA and two-stage differential opamp.

Fig. 13.   Photograph of the chip.

VI. CMOS MICROFLUIDICS INTEGRATION AND EXPERIMENTAL SETUP

The cells are typically dispersed in saline solution that can corrode Al wire-bonds and pads. However, the chip has to be connected to external circuit components and the flow of cells also requires that the chip is in flush with the substrate holding it. In addition, the chip generates heat that should be dissipated out to limit the final temperature to less than 37 °C. The following process steps are used to integrate the CMOS chip with the microfluidic channel to address these challenges.

First, a cavity is created in a holder ENIG-PCB. The CMOS chip is placed upside down and is aligned to the center of the cavity using a laser cut polystyrene structure. A conducting polymer (Coolpoly E3607) piece is placed in the cavity on top of the chip. By applying pressure of 720 psi at 95 °C in a hot embosser for 5 min, the polymers melt and conform with the cavity, holding the chip in place. After the setup has cooled to room temperature, the chip is subsequently wire-bonded to the PCB and covered with epoxy [see Fig. 14(a)].

For fabricating the PDMS microchannel, we have designed a 3-D printed mold that includes cavities for wire-bonds. The microfluidic channel (200 μm wide and 100 μm high) is subsequently treated with O_2 plasma to make it hydrophilic. The microchannel is aligned over the sensor on the chip and

an acrylic piece is used to press-fit the microfluidic channel against the chip to avoid leakage as shown in Fig. 14(a). The fabricated flow cytometer is shown in Fig. 14(b).

The complete cytometer prototype is connected to a sister PCB to provide dc bias, off-chip gain, power supply, digitization and data acquisition through an FPGA. The cytometer cartridge along with sister PCB is firmly mounted on a clamp and powered with a 5-V external dc supply as shown in Fig. 14(c). A microscope is used to visualize the flow of cells through the microfluidic channel. Flow cytometry experiments are carried out by placing a 50-μL drop of sample at the inlet of the cytometer and it is vertically driven by gravity through the microfluidic channel. Matched filtering is done offline for I and Q channels separately and the angle is computed after thresholding. It is important to note here that the shape of the matched filter impulse response [shown in Fig. 4(b)] is determined by the layout of the sensor (particularly the excitation coil) and its duration is determined time-of-flight of the cell over the sensor. To first order, it does not depend on the class and number of magnetic labels bound on a cell. In this paper, we have manually chosen the impulse response duration to maximize the SNR.

We have used a weak magnet (10 mT) beneath the CMOS chip to pull the beads closer to the sensor surface (vertical magnetophoresis). It is shown in [23] that on-chip current wires can be used to achieve horizontal focusing efficiency upto 98%, however, this technique is not used for the experimental results presented in this paper.

VII. MEASUREMENT RESULTS

A. Dynabead Detection

Dynabeads made of iron oxide are used for benchmarking the cytometer. These magnetic beads have an average diameter of 4.5 μm with well characterized magnetic properties [31]. 50 μL of DI water is loaded at the inlet of the cytometer and offset cancellation is performed as it flows through the cytometer. Next, about 50 μL of the Dynabead sample (8×10^6
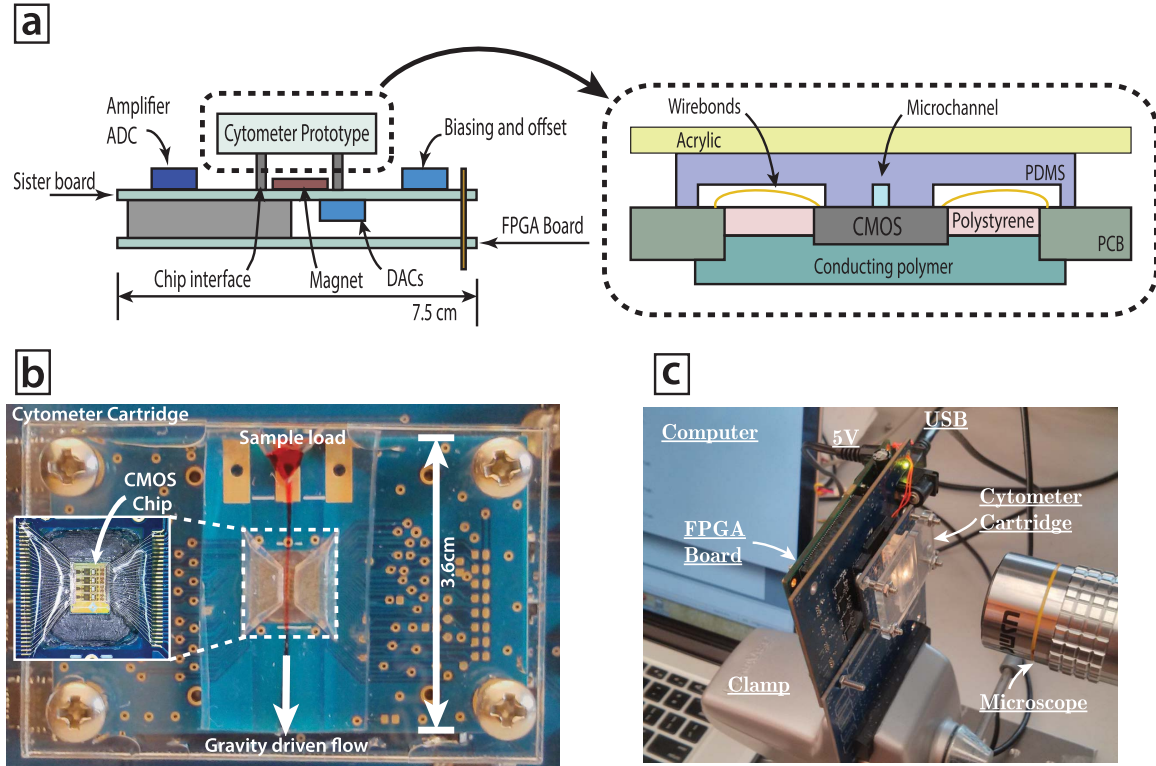
Fig. 14.   (a) Schematic of CMOS integrated with microfluidics. (b) Fabricated flow cytometer. (c) Experimental setup.
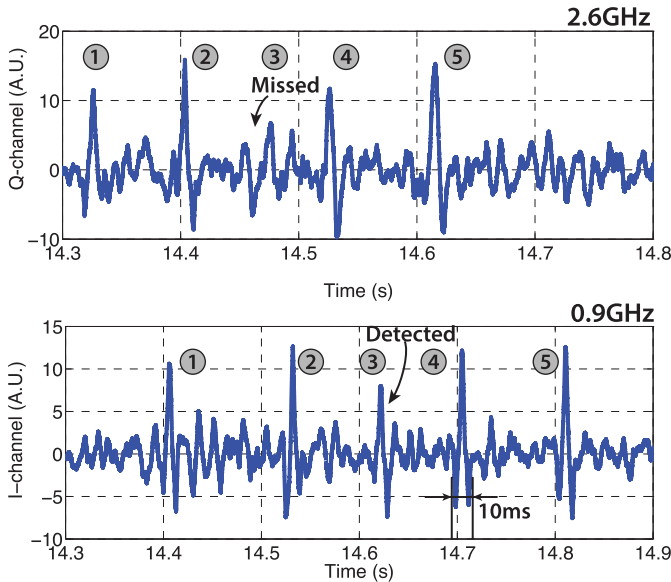

Fig. 15.   Detection of Dynabeads by two frequency channels.

beads/mL) is loaded at the inlet and the data are acquired as these particles flow over the sensor. As seen from Fig. 1(a), at 0.9 GHz, the χ' of Dynabeads (I-channel) is two times higher than χ'' (Q-channel), and hence, the 0.9-GHz I-channel is considered for detection. While at 2.6 GHz, the χ'' (Q-channel) is 3.3 times higher than χ' (I-channel), and hence, the 2.6-GHz-Q-channel is considered for detection. Fig. 15 shows the detection of 4.5-μm Dynabeads with an average SNR of 21.3 dB for 0.9-GHz-I-channel and 19.9-dB for 2.6-GHz-Q-channel after matched filtering.

Furthermore, it can be seen that a particle missed on the 2.6-GHz channel is detected by the 0.9-GHz channel.

Dynabeads can be detected upto 1.4 μm away from the sensor surface for 8.6-dB SNR on 0.9-GHz channel.

B. Cell Labeling and Detection

We have chosen SKBR-3 cancer cells which over-express EpCAM antigen and they have a typical diameter of 15 μm. The labeling of these cells is carried out in a two-step process. First, the EpCAM antigen on the cell surface is conjugated with biotinylated anti-EpCAM (CD326) antibody. Second, the biotin is conjugated with magnetic labels coated with streptavidin.

We start with a Petri dish containing about 5×10^6 SKBR-3 cells. A solution buffer is prepared by mixing 2 mL of 7.5% bovin serum albumin with 28-mL PBS. About 2 mL of 0.25% trypsin is mixed with 8 mL of PBS. A 3 mL of this mixture is used to wash the cells and rest of it is added to the cell plate. After incubation at 37 °C for 5 min until most cells have detached from the plate, they are transferred to a tube for centrifugation. Subsequently, the cell palette is resuspended in a mix of 1.5 μL of stock biotinylated anti-EpCAM antibody and 0.6 mL of buffer solution and incubated for 20 min at 37 °C with gentle mixing. Now, most of the EpCAM antigens on the cell have been conjugated with biotinylated antibody. The final step of magnetic labeling is carried out by adding 15 μL of 10 mg/mL streptavidin coated $MnFe_2O_4$ magnetic labels of size 800 nm–1 μm (from OceanNanotech Inc.) and incubated for another 20 min with gentle mixing. The labeled cells shown in Fig. 16(a) are then used for flow cytometry experiments within 2 h. Since many labels (size ≤ 1 μm) bind to a single cell (size ≈ 15 μm), the SNR_{cell} > detection threshold > SNR_{label} ensuring the detection of only the labeled cells by the receiver. However,
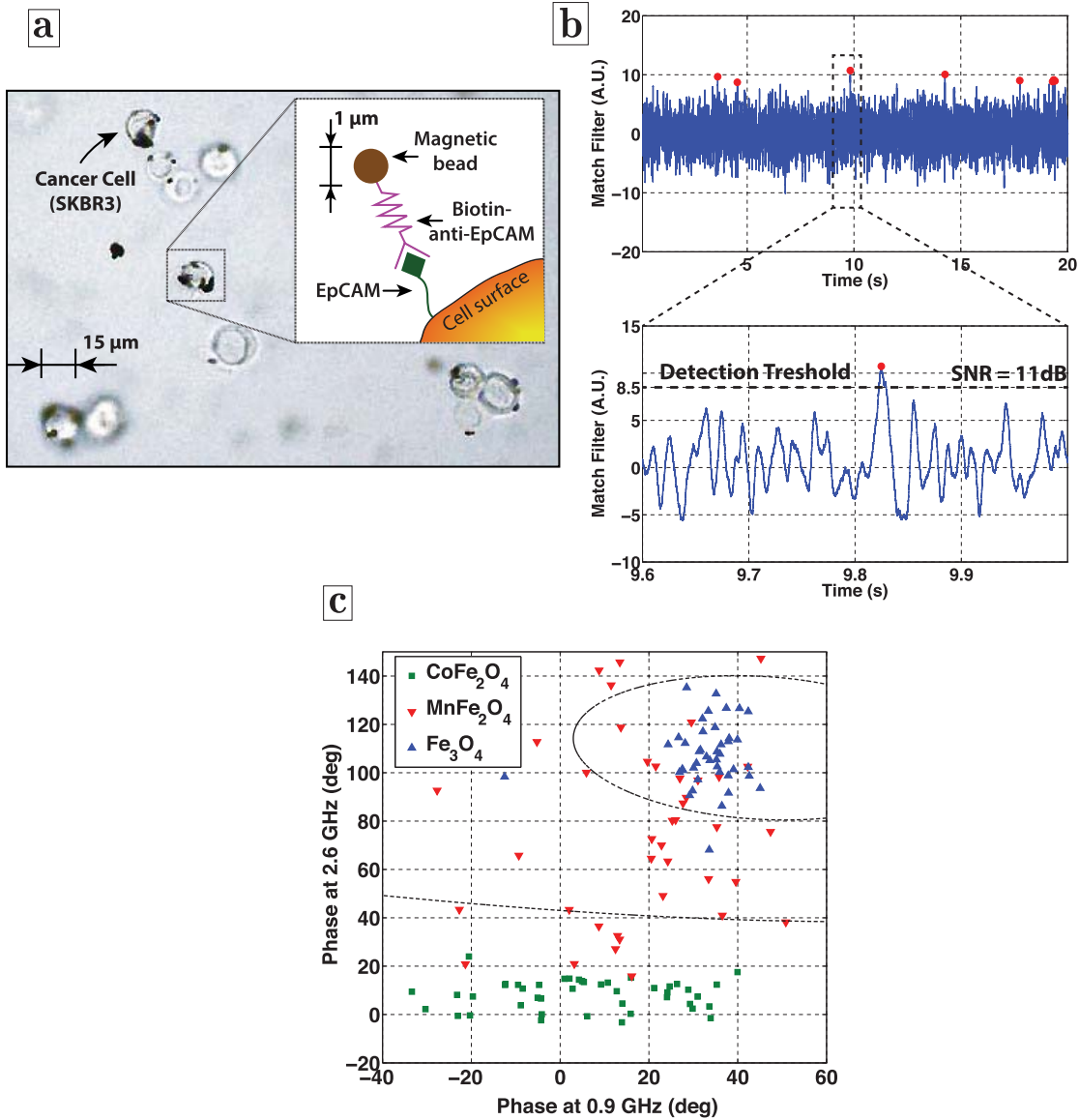
Fig. 16. (a) Magnetic labeling of SKBR3 cells. (b) Detection of magnetically labeled cells by the cytometer. (c) Classification of three label classes by the flow cytometer.

use of excess magnetic labels can form clumps and lead to false detection during flow experiments. Likewise, free unbound labels in the sample can cause excess shot-noise affecting the SNR. In this paper, no unbound label removal step is used, the necessary concentration of magnetic labels is determined experimentally.

Fig. 16(b) shows the match filtered output from cell flow experiments. It can also be seen here that the noise floor is higher than in Fig. 15 due to the higher conductivity of saline solution than DI water. The detection threshold is set to 11 dB to give a CV = 3.2% better than the design value of CV = 4%. Titration experiments to determine counting efficiency and average count rate for our device were affected by cell settling at the inlet and stiction to microchannel walls. This microfluidic challenge has to be addressed in the future by designing smooth transitions in microfluidic channel cross section, long off-chip horizontal magnetophoretic focusing structures, and suitable microchannel surface functionalization

in order to benchmark this magnetic cytometer against a reference instrument such as an optical cytometer. In addition, it would be useful to determine a cell's antigen expression from its signal strength. Considering the challenges mentioned in Section IV-B3, it is difficult to precisely quantify the number of labels conjugated to a given cell and consequently its antigen expression. However, if we assume that $\chi = 0.1$ at 0.9 GHz for 1-μm-$MnFe_2O_4$ labels, then an *average* of 15 labels (calculated) is bound on a cell to give SNR of 11 dB.

C. Label Classification

For label classification experiments, biotin coated 8-μm polymer particles (Bangs Laboratories Inc.), acting as cell proxies, are labeled with 1-μm $MnFe_2O_4$ and $CoFe_2O_4$ magnetic labels using streptavidin-biotin chemistry. The labeled cell proxies are carried over the sensor in saline. The detection threshold is set to SNR of 11 dB after matched filtering.

The peak amplitude of the pulse of in-phase channel (or quadrature-phase channel) that exceeds the detection

TABLE I
COMPARISON WITH PRIOR CHIP SCALE MAGNETIC FLOW CYTOMETERS

	Issadore et. al. 2012	Helou et. al. 2013	ISSCC 2014 (Murali et. al.)	This work
Technology	PHEMT	GMR	180nm CMOS	65nm CMOS
Sensor	μHall detector	GMR	Spiral transformer	Spiral transformer
Sensor integration	N/A	N/A	On-chip	On-chip
Application	Flow cytometry	Flow cytometry	Flow cytometry	Flow cytometry
Excitation field frequency	DC	DC	1.2GHz	0.9GHz and 2.6GHz
Other components	0.5T Magnet	0.2T Magnet	None	10mT Magnet
Labels	$MnFe_2O_4$	FeO_x	FeO_x and Co	$MnFe_2O_4$, Fe_2O_3 and $CoFe_2O_4$
Separate Label Classes	3	1	2	3
Detection Time	0.02 ms	40 ms	20 ms	10ms

threshold is used along with the corresponding amplitude of quadrature-phase channel (or in-phase channel) to determine the phase of the signal. Fig. 16(c) shows the phase response obtained for the magnetic labels at both the frequencies. Also shown in Fig. 16(c) is the phase of Dynabeads (Fe_3O_4). It can be seen in Fig. 1(c) that the phase plots between $MnFe_2O_4$ and Fe_3O_4 are similar; hence, their scatter plots in Fig. 16(c) overlap. However, it can also seen in Fig. 1(c) that there is significant phase difference (nearly 80°) between Fe_3O_4 and $CoFe_2O_4$ at 2.6 GHz leading to their well separated scatter plots in Fig. 16(c). Using equal prior probabilities of magnetic labels, we get a classification accuracy of 74% using phase data at 2.6 GHz (with only linear a discriminator). However, the accuracy improves to 87% by using phase data at both 0.9 GHz and 2.6 GHz (with a quadratic discriminator).

Table I compares this work to prior magnetic cytometers, which do not fully integrate a complete flow cytometer in CMOS technology. Encapsulation of multifrequency CMOS magnetic sensor chip into a microfluidic cartridge enables the detection of multiple label classes with this miniature device.

VIII. CONCLUSION

We have presented a CMOS magnetic flow cytometer fabricated in 65-nm CMOS technology. On chip receiver circuitry demodulate the signal from a pickup coil enclosing a differential excitation coil operating at 0.9 and 2.6 GHz. The CMOS chip is integrated within the microfluidic channel using the hot-embossing technique. The operation of the chip is verified for 4.5-μm Dynabeads and magnetically labeled cells. Measurement results for the classification of magnetic labels made of different materials are also presented.

ACKNOWLEDGMENT

REFERENCES

[1] M. Brown and C. Wittwer, "Flow cytometry: Principles and clinical applications in hematology," *Clin. Chem.*, vol. 46, no. 8, pp. 1221–1229, 2000.

[2] J.-C. Chien and A. M. Niknejad, "Oscillator-based reactance sensors with injection locking for high-throughput flow cytometry using microwave dielectric spectroscopy," *IEEE J. Solid-State Circuits*, vol. 51, no. 2, pp. 457–472, Feb. 2016.

[3] H. Song et al., "A microfluidic impedance flow cytometer for identification of differentiation state of stem cells," *Lab Chip*, vol. 13, no. 12, pp. 2300–2310, 2013.

[4] N. Watkins, B. M. Venkatesan, M. Toner, W. Rodriguez, and R. Bashir, "A robust electrical microcytometer with 3-dimensional hydrofocusing," *Lab Chip*, vol. 9, no. 22, pp. 3177–3184, 2009.

[5] K.-H. Lee, J. Nam, S. Choi, H. Lim, S. Shin, and G.-H. Cho, "A CMOS impedance cytometer for 3D flowing single-cell real-time analysis with $\Delta\Sigma$ error correction," in *IEEE Int. Solid-State Circuits Conf. (ISSCC) Dig. Tech. Papers*, Feb. 2012, pp. 304–306.

[6] C. Jun-Chau, M. Anwar, Y. Erh-Chia, L. P. Lee, and A. M. Niknejad, "A 6.5/11/17.5/30-GHz high throughput interferometer-based reactance sensors using injection-locked oscillators and ping-pong nested chopping," in *Symp. VLSI Circuits Dig. Tech. Papers*, Jun. 2014, pp. 1–2.

[7] S. Emaminejad, M. Javanmard, R. W. Dutton, and R. W. Davis, "Microfluidic diagnostic tool for the developing world: Contactless impedance flow cytometry," *Lab Chip*, vol. 12, no. 21, pp. 4499–4507, 2012.

[8] S. Gawad, K. Cheung, U. Seger, A. Bertsch, and P. Renaud, "Dielectric spectroscopy in a micromachined flow cytometer: Theoretical and practical considerations," *Lab Chip*, vol. 4, no. 3, pp. 241–251, 2004.

[9] C. Küttel, E. Nascimento, N. Demierre, T. Silva, T. Braschler, P. Renaud, and A. G. Oliva, "Label-free detection of *Babesia bovis* infected red blood cells using impedance spectroscopy on a microfabricated flow cytometer," *Acta Tropica*, vol. 102, no. 1, pp. 63–68, Apr. 2007.

[10] M. M. Varma. (2015). "Limitations of label-free sensors in serum based molecular diagnostics." [Online]. Available: https://arxiv.org/abs/1505.01032

[11] J. Loureiro, P. Z. Andrade, S. Cardoso, C. L. da Silva, J. M. Cabral, and P. P. Freitas, "Magnetoresistive chip cytometer," *Lab Chip*, vol. 11, no. 13, pp. 2255–2261, 2011.

[12] M. Helou et al., "Time-of-flight magnetic flow cytometry in whole blood with integrated sample preparation," *Lab Chip*, vol. 13, no. 6, pp. 1035–1038, 2013.

[13] Y. R. Chemla *et al.*, "Ultrasensitive magnetic biosensor for homogeneous immunoassay," *Proc. Nat. Acad. Sci. USA*, vol. 97, no. 26, pp. 14268–14272, 2000.

[14] D. Issadore *et al.*, "Ultrasensitive clinical enumeration of rare cells *ex vivo* using a micro-Hall detector," *Sci. Transl. Med.*, vol. 4, no. 141, p. 141ra92, 2012.

[15] C. Sideris and A. Hajimiri, "An integrated magnetic spectrometer for multiplexed biosensing," in *IEEE Int. Solid-State Circuits Conf. (ISSCC) Dig. Tech. Papers*, Feb. 2013, pp. 300–301.

[16] H. Wang, Y. Chen, A. Hassibi, A. Scherer, and A. Hajimiri, "A frequency-shift CMOS magnetic biosensor array with single-bead sensitivity and no external magnet," in *IEEE Int. Solid-State Circuits Conf. (ISSCC) Dig. Tech. Papers*, Feb. 2009, pp. 438–439.

[17] S. Gambini *et al.*, "A CMOS 10kpixel baseline-free magnetic bead detector with column-parallel readout for miniaturized immunoassays," in *IEEE Int. Solid-State Circuits Conf. (ISSCC) Dig. Tech. Papers*, Feb. 2012, pp. 126–128.

[18] P. C. Fannin, "Wideband measurement and analysis techniques for the determination of the frequency-dependent, complex susceptibility of magnetic fluids," in *Adv. in Chem. Phys.*, vol. 104, pp. 181–292, 1998.

[19] P. C. Fannin, T. Relihan, and S. W. Charles, "Experimental and theoretical profiles of the frequency-dependent complex susceptibility of systems containing nanometer-sized magnetic particles," *Phys. Rev. B*, vol. 55, no. 21, p. 14423, 1997.

[20] *BD Accuri C6 Flow Cytometer Technical Specifications*, accessed on Aug. 9, 2016. [Online]. Available: https://www.bdbiosciences.com

[21] L. A. Currie, "Limits for qualitative detection and quantitative determination. Application to radiochemistry," *Anal. Chem.*, vol. 40, no. 3, pp. 586–593, 1968.

[22] B. E. Boser and P. Murali, "Flow cytometer-on-a-chip," in *Proc. IEEE Biomed. Circuits Syst. Conf. (BioCAS)*, Oct. 2014, pp. 480–483.

[23] V. Iyer, P. Murali, J. Paredes, D. Liepmann, and B. Boser, "Encapsulation of integrated circuits in plastic microfluidic systems using hot embossing," in *Proc. Transducers–18th Int. Conf. Solid-State Sens., Actuators Microsyst.*, Jun. 2015, pp. 1822–1825.

[24] M. A. der Mauer, "Magento-phoresis in microfluidic devices," M.S. thesis, ETH Zürich, Zürich, Switzerland, 2016.

[25] A. Stogryn, "Equations for calculating the dielectric constant of saline water (correspondence)," *IEEE Trans. Microw. Theory Techn.*, vol. 19, no. 8, pp. 733–736, Aug. 1971.

[26] S. B. Field and C. C. Morris, "The relationship between heating time and temperature: Its relevance to clinical hyperthermia," *Radiotherapy Oncol.*, vol. 1, no. 2, pp. 179–186, 1983.

[27] A. A. Abidi, "Direct-conversion radio transceivers for digital communications," *IEEE J. Solid-State Circuits*, vol. 30, no. 12, pp. 1399–1410, Dec. 1995.

[28] B. Razavi, "Design considerations for direct-conversion receivers," *IEEE Trans. Circuits Syst. II, Analog Digit. Signal Process.*, vol. 44, no. 6, pp. 428–435, Jun. 1997.

[29] R. Przybyla, "Ultrasonic 3D rangefinder on a chip," Ph.D. dissertation, Elect. Eng. Comput. Sci. Dept., Univ. California, Berkeley, Berkeley, CA, USA, May 2015. [Online]. Available: http://www.eecs.berkeley.edu/Pubs/TechRpts/2015/EECS-2015-27.html

[30] P. R. Gray, P. J. Hurst, R. G. Meyer, and S. H. Lewis, *Analysis and Design of Analog Integrated Circuits*. Hoboken, NJ, USA: Wiley, 2001.

[31] G. Fonnum, C. Johansson, A. Molteberg, S. Mørup, and E. Aksnes, "Characterisation of Dynabeads by magnetization measurements and Mössbauer spectroscopy," *J. Magn. Magn. Mater.*, vol. 293, no. 1, pp. 41–47, 2005.

Pramod Murali (S'15–M'16) received the B.Tech. degree in electronics and communication engineering from the National Institute of Technology Karnataka, Surathkal, India, in 2009, the M.E. degree in microelectronic systems from the Indian Institute of Science (IISc), Bengaluru, India, in 2011, and the Ph.D. degree in electrical engineering from the University of California at Berkeley, Berkeley, CA, USA, in 2015.

He was with the Center for NanoScience and Engineering, IISc, from 2011 to 2012, as a Project Associate, where he developed a CMOS volatile organic gas sensor system. He is currently a Research Engineer with the Bosch Research and Technology Center, Palo Alto, CA, USA. His current research interests include ultrasound-based diagnostics, point-of-care biosensors, LiDAR technologies, and connected sensor systems for IoE.

Dr. Murali received the The Alumni Award from IISc in 2011, the Outstanding Designer Award by Analog Devices Inc., in 2014, and the IEEE Solid State Circuits Society Predoctoral Achievement Award in 2015.

Ali M. Niknejad (F'13) received the Ph.D. degree in electrical engineering from the University of California at Berkeley, Berkeley, CA, USA, in 2000.

He is currently a Professor and the Faculty Director of the Berkeley Wireless Research Center, University of California at Berkeley. He is a Co-Founder of HMicro, Bengaluru, India, and the Inventor of the Reach Technology, which has the potential to deliver robust wireless solutions to the healthcare industry. His current research interests include wireless communications, biomedical sensors and imaging, analog, RF, mixed-signal, millimeter-wave circuits, device physics and compact modeling, and numerical techniques in electromagnetics.

Dr. Niknejad was a recipient of the 2012 ASEE Frederick Emmons Terman Award for his textbook on electromagnetics and RF integrated circuits. He was a co-recipient of the IEEE International Solid-State Circuits Conference (ISSCC) in 2013 and the 2010 Jack Kilby Awards for Outstanding Student Papers, and also a co-recipient of the Outstanding Technology Directions Paper at ISSCC 2004 for codeveloping a modeling approach for devices up to 65 GHz.

Bernhard E. Boser (F'03) received the Diploma degree in electrical engineering from the Swiss Federal Institute of Technology, Zürich, Switzerland, in 1984, and the M.S. and Ph.D. degrees from Stanford University, Stanford, CA, USA, in 1985 and 1988, respectively.

From 2005 to 2006, he served as the Chief Scientist and designed the company's first microelectro-mechanical systems (MEMS) oscillator circuit. From 2005 to 2006, he was a Visiting Professor with the Swiss Federal Institute of Technology. Since 1988, he has been a member of Technical Staff with the Adaptive Systems Department, AT&T Bell Laboratories, Murray Hill, NJ, USA. In 1992, he joined the Department of Electrical Engineering and Computer Sciences, University of California at Berkeley, Berkeley, CA, USA, as a Faculty Member, where he also serves as a Co-Director of the Berkeley Sensor & Actuator Center, Berkeley, CA, and the UC Berkeley Swarm Lab, Berkeley, CA. In 2004, he co-founded SiTime, Santa Clara, CA, USA, a fabless mixed signal semiconductor company that offers MEMS-based silicon timing solutions replacing legacy quartz products. With 85% market share and over 35 million devices shipped, SiTime is the leader in this field and driving the 5 billion timing markets transition to silicon-based solutions. He and his co-workers' accomplishments include differential capacitive readout techniques for MEMS accelerometers and gyroscopes, now used in the majority of commercial inertial sensors. The pioneering work on sigma–delta analog–digital converters, ultralow power successive approximation converters, and digitally assisted analog circuits has stimulated research and products in mixed-signal integrated circuits. His paper "Training Algorithm for Optimal Margin Classifiers," published in 1992 by the ACM Workshop on Computational Learning Theory is the first description of the Support-Vector Algorithm, SVM, a classification technique that has become widely used in applications ranging from financial prediction to bioinformatics and data analytics. His current research interests include analog and mixed signal circuits, with special emphasis on sensor and actuator interfaces.

Dr. Boser has served on the program committees of the International Solid-State Circuits Conference, the Transducers Conference, the VLSI Symposium, and the Solid-State Sensor and Actuator Workshop. He has also served the IEEE Solid-State Circuits Society as the Editor-in-Chief of the *Journal of Solid-State Circuits*, the Chair of the Publications Committee, and the President of the Publications Committee from 2010 to 2011.